Supporting Information

Taniguchi et al. 10.1073/pnas.1218025110

SI Materials and Methods

Plasmids, Cells, and Culture Conditions. Expression vectors for GFP and RFP that harbor a hygromycin resistance cassette were first constructed. Briefly, pA15GFP(S65T) (1) was cut with XbaI and HindIII to obtain an actin15 promoter-GFP-act8term fragment that was ligated to pHygTm(plus)/pG7 [a kind gift from M. Fukuzawa, (Hirosaki University, Hirosaki, Aomori, Japan)] linearized with the same enzymes. To obtain pHygRFPmars, the resulting vector pHygGFP was further cut with ClaI and XhoI to replace GFP with RFPmars (2) with or without the stop codon. The mRFPmars fragment was obtained by PCR, using vector 339-3 (Dicty Stock Center plasmid ID no. 1 from A. Müller-Taubenberger, Ludwig Maximilians University of Munich, Munich, Germany) as a template. To construct PI3K-RFP, the first 1,533 bp of the *pikA* gene encoding PI3kinase was PCR amplified from genomic DNA, using primers ATCGATATGAATAGTATTGAAAGTTCTTCTA (pikA_F2ClaI) and TGATGATGATGCTGATGCTG (pikA_1533R). Finally we ligated the *pikA* fragment to pHygRFPmars to obtain PI3K-RFP.

To express actin-binding protein LimE fused to GFP, expression vector pA15GFPLimEΔcoil was constructed. We first removed the stop codon of GFP in pA15GFP(S65T) to obtain pA15GFP(TAA−). Following an earlier report (3), we used the first 145 bp of the *limE* gene to image F-actin. PCR was performed using primers CTCGAGGGTGGTTCAGGTGGTTCAATGTCTGCTTCAG (GGSLimE_F3) and CTCGAGACCAGTTGGTTGACCATCAGCA (LimE_R1). The PCR products were cloned and sequenced in the pCR-BluntII-TOPO vector. The confirmed DNA fragment was excised using ClaI and XhoI and ligated to pA15GFP(TAA−) to obtain pA15GFPLimEΔcoil. PHcrac-RFP and PTEN-GFP were used as markers for phosphatidylinositol (3,4,5)-trisphosphate (PIP3) and phosphatidylinositol (4,5)-bisphosphate (PIP2), respectively. An expression vector with a hygromycin resistance cassette that harbors the PH domain of CRAC fused to mRFP1 was a gift from R. Firtel (University of California, San Diego, CA). pPTEN-GFP (plasmid catalog no. 66 from P. Devreotes, Johns Hopkins University, Baltimore, Maryland), a null mutant of pirA gene encoding PIR121 (*pirA*$^-$) (strain ID DBS0236780 from R. Insall, Beatson Institute for Cancer Research, Glasgow, UK), a double knockout strain of genes encoding PI3kinase pikA and pikB (*pikA*$^-$/*pikB*$^-$) (strain ID DBS0236766 from R. Firtel), and a null mutant of phosphatase PTEN (*pten*$^-$) (strain ID DBS0236830 from P. Devreotes) were obtained from the Dicty Stock Center.

Laboratory wild-type strain AX4 and mutant strains of *Dictyostelium discoideum* were transformed and cloned following a standard electroporation protocol (4). Cells were cultured and shaken at 22 °C in liquid medium containing 1% peptone, 0.7% yeast extract, 1.5% (wt/vol) D-glucose, 10 mM KH_2PO_4, 0.24 mM Na_2HPO_4, 1× antibiotic antimycotic mix (Gibco), 40 ng/mL vitamin B12, and 80 ng/mL folic acid. In addition, 60 μg/mL hygromycin B, 10 μg/mL G418, and 10 μg/mL Blasticidin S were added appropriately for selection. For live cell imaging, exponentially growing cells were washed twice and suspended in developmental buffer (DB) (10 mM KH_2PO_4, 10 mM Na_2HPO_4, 2 mM $MgSO_4$, 0.2 mM $CaCl_2$, pH 6.5) at a cell density of 1.0×10^7 cells/mL and shaken for 4 h at 22 °C.

Live Cell Imaging. After 4 h of nutrient depletion, cells were washed twice, resuspended in DB, and plated on a glass-bottom dish (MatTek) at a cell density of 1.0×10^3 cells/cm^2. Both LY294002 (L9908-1MG; Sigma) and latrunculin A (125-04363; Wako) were dissolved in dimethyl sulfoxide (DMSO) and applied to the cell suspension at least 30 min before observation. An equivalent amount of DMSO alone was used for mock controls. The observation dish was assembled on an inverted microscope (IX-81; Olympus) equipped with a confocal multibeam scanning unit (CSU-X1; Yokogawa), laser sources for blue light (488 nm, 30 mW; Melles Griot) and green light (561 nm, 25 mW; Melles Griot) excitation, oil immersion objectives (60× PlanApo N, N.A. 1.42, or 100× UPlanSApo, N.A. 1.40; Olympus), and an Electron Multiplying CCD camera (QuantEM:512SC; Photometrics). To detect GFP and RFP fluorescence, a bandpass filter (510–550 nm; BA510-550, Olympus) and a broad spectrum filter (>575 nm; BA575IF, Olympus) were used, respectively. The focal plane was chosen in the vicinity of the cell membrane ∼200 nm from the glass surface. Fluorescence intensity images of 512 × 512 pixels with 8-bit depth were acquired separately for GFP and RFP with a delay of ∼30 ms at 6- to 12-s intervals. Data were acquired using the MetaMorph software (Molecular Devices) and stored in Tagged Image File Format (TIFF) files.

Image Processing and Phase Analysis. All images were processed using MATLAB 2010b (MathWorks). To reduce noise, digitally acquired fluorescence intensity was averaged using the nonlocal means method (5), which exploits spatial correlation in the whole image. Because each pixel value is determined as a weighted average of other pixels with a related surrounding neighborhood, the method allows removal of noise without losing fine structures—most importantly, spatial phase singularities in our study. The nonlocal means algorithm requires one to set a few parameters: search window size, similarity window size, and a filtering parameter h (5). We fixed a search window to 21 × 21 pixels and a similarity window to 7 × 7 pixels, which approximately equals 4×4 μm^2 and 1.3×1.3 μm^2, respectively. The filtering parameter h typically ranged from 0.1σ to 0.5σ, where σ is the SD of the intensity distribution of the entire image (a region of interest under analysis). Results of our analysis were robust to minor changes in these parameters.

To extract phase of PIP3 waves at each point in space, we first applied wavelet transform using a complex Morlet function

$$\psi(t) \equiv \frac{1}{\sqrt{2\pi}} \exp(i\omega t) \exp\left(-\frac{t^2}{2}\right) \qquad [S1]$$

to time series data of PHcrac-RFP fluorescence intensity taken from each pixel. To satisfy the admissibility condition, we chose $\omega = 6$. A major peak in the power spectra was determined as the dominant frequency mode. Phase was obtained by calculating the arctangent of the ratio of real and imaginary parts of complex wavelet coefficients of the dominant mode. Phase singularity was characterized in terms of topological charge, n_t, which was defined by

$$n_t = \frac{1}{2\pi} \oint_C \nabla\psi \cdot \mathbf{dl} = \begin{cases} +1 \\ -1 \end{cases}, \qquad [S2]$$

where ψ is the local phase, and the line integral is taken over a path on a circle c surrounding the phase singularity point.

Cross-Correlations Analysis. Cross-correlation between the PHcrac-RFP signal intensity at time t and velocity of membrane extension ($\partial r/\partial t$) at time $t + \tau$ at each point along the cell edge (Fig. S1*C*) was measured. Fig. S1*D* (*Left*) displays the average cross-corre-

lations as a function of τ. Correlation takes the maximum value 0.20 at $\tau = 0.5$ min, indicating that cell protrusion velocity peaks at ~30 s after the arrival of PIP3 waves. The statistical significance of this correlation was checked by comparison with bootstrap samples where the phases in Fourier modes of the original data were scrambled (6). Our null hypothesis is that these randomized data are sufficient to explain the maximum value of the cross-correlation. The distribution of the maxima was evaluated from 5,000 bootstrap samples, and none exceeded the maximum of the original data, validating that the cross-correlations in the original data are statistically significant. We also measured cross-correlation between signal intensities of PHcrac-RFP at time t and phosphatase and tensin homolog (PTEN) at time $t + \tau$, as shown in Fig. S1*D* (*Right*). PIP3 and PTEN exhibit negative correlation around $\tau = 0$. Statistical significance of the minimum value in the cross-correlation was also confirmed by the bootstrap test.

SI Text

Reaction Diffusion Model. A mathematical model was analyzed to determine the key reaction kinetics in the phosphoinositides' signaling (7) responsible for the observed wave behaviors. We considered the following reactions (Fig. S4*A*): (*i*) PI3K in the cytoplasm is recruited to the basal membrane and catalyzes phosphorylation of phosphatidylinositol (4,5)-bisphosphate (PIP2) to phosphatidylinositol (3,4,5)-trisphosphate (PIP3) (8). The recruitment and activation of PI3K is enhanced by PIP3 possibly through accumulation of F-actin (8, 9). (*ii*) Phosphatase and tensin homolog (PTEN) in the cytoplasm is recruited to the site of PIP2 at the membrane (10), which then mediates dephosphorylation of PIP3 to PIP2. (*iii*) PIP2 is produced and degraded at constant rates. (*iv*) PIP3 is degraded at a constant rate. Simple rate equations with respect to the concentrations of PIP2 ([PIP2]), PIP3 ([PIP3]), PI3K ([PI3K$_m$]), and PTEN ([PTEN$_m$]) at the basal membrane are

$$\begin{aligned}
\frac{d[PIP2]}{dt} &= -k_1[PI3K_m][PIP2] + k_2[PTEN_m][PIP3] \\
&\quad + k_4 - k_5[PIP2] \\
\frac{d[PIP3]}{dt} &= k_1[PI3K_m][PIP2] - k_2[PTEN_m][PIP3] \\
&\quad - k_3[PIP3] \\
\frac{d[PI3K_m]}{dt} &= k_6[PIP3]^2[PI3K_c] - k_7[PI3K_m] \\
\frac{d[PTEN_m]}{dt} &= k_8[PIP2][PTEN_c] - k_9[PTEN_m].
\end{aligned} \quad \textbf{[S3]}$$

Here [PI3K$_c$] and [PTEN$_c$] represent concentrations of PI3K and PTEN in the cytosol, respectively. The kinetic parameter k_6 defines strength of the positive feedback from PIP3 to PI3K. The underlying intermediate signaling steps that realize this feedback are presently unknown. Here, we assumed that these steps are fast and thus can be eliminated after steady-state approximation.

The reaction scheme is similar to that proposed earlier (11, 12) that also includes the F-actin–mediated positive feedback. The current model, however, does not include the hypothetical PIP3-PTEN–mediated regulation that provides an additional positive feedback (11, 12). As for the necessary negative feedback, both the earlier model (11, 12) and the current model suggest that reduction in PTEN/PIP2 plays the main inhibitory role such that the scheme follows the so-called "substrate-depletion"-type mechanism in line with the fact that PIP3 and PTEN appear to be antiphase. In animal cells, another type of actin waves of smaller wavelength that propagate inward from the periphery appears to be driven by an alternative mechanism, where F-actin plays an inhibitory role on the activator (Hem-1) membrane association (13). In the present model, we do not assume such negative regulation from F-actin to PIP3 generation.

Because molecules in the cytosol diffuse hundreds times faster than those at the membrane (14, 15), the concentrations of PI3K and PTEN in the cytoplasm were assumed to be uniform in space. We imposed that the total amounts of PI3K and PTEN, i.e., both the cytosolic and membrane fractions combined, are preserved during observations. Therefore,

$$\begin{aligned}
\int_\Omega [PI3K_m]dx + [PI3K_c]A &= c_K A \\
\int_\Omega [PTEN_m]dx + [PTEN_c]A &= c_P A.
\end{aligned} \quad \textbf{[S4]}$$

A is the area of a cell, Ω represents a region occupied by the basal membrane, and c_K and c_P represent total amount of PI3K and PTEN, respectively. We further assumed that phosphorylation and dephosphorylation steps are fast compared with other reactions. As a result, concentrations of PI3-kinase and PTEN at the basal membrane are enslaved to [PIP3] and [PIP2], respectively. Thus

$$\begin{aligned}
[PI3K_m] &= \frac{c_K[PIP3]^2}{k_7/k_6 + A^{-1}\int_\Omega [PIP3]^2 dx} \\
[PTEN_m] &= \frac{c_P[PIP2]}{k_9/k_8 + A^{-1}\int_\Omega [PIP2]dx}.
\end{aligned} \quad \textbf{[S5]}$$

By including diffusion of phosphatidylinositols in the basal membrane, we obtained the following partial differential equations with global integrals. Namely,

$$\begin{aligned}
\frac{\partial U}{\partial t} &= D_U \Delta U - \frac{\alpha U V^2}{K_K + A^{-1}\int_\Omega V^2 d\mathbf{x}} + \frac{\beta U V}{K_P + A^{-1}\int_\Omega U dx} + S - \gamma U \\
\frac{\partial V}{\partial t} &= D_V \Delta V + \frac{\alpha U V^2}{K_K + A^{-1}\int_\Omega V^2 d\mathbf{x}} - \frac{\beta U V}{K_P + A^{-1}\int_\Omega U dx} - \mu V.
\end{aligned} \quad \textbf{[S6]}$$

Here, $U = [PIP2]$ and $V = [PIP3]$. The parameters are defined as $\alpha = c_K k_1$, $\beta = c_P k_2$, $K_K = k_7/k_6$, $K_P = k_9/k_8$, $S = k_4$, $\gamma = k_5$, and $\mu = k_3$.

Numerical simulations were performed in a 2D circular region for immotile cells (Fig. 4 *A*–*D*). We assumed that PIP2 and PIP3 can escape from the region of our interest at the cell boundary. Therefore, we adopted the following absorbing boundary conditions:

$$\begin{aligned}
-D_U \nabla U \cdot \mathbf{n} - \chi_u U = 0 \\
-D_V \nabla V \cdot \mathbf{n} - \chi_v V = 0.
\end{aligned} \quad \textbf{[S7]}$$

Here $\mathbf{n}$ indicates the unit normal vector at the boundary of a cell region. The second terms represent the escape rates of PIP2 and PIP3 at the cell boundary where χ_u and χ_v are the absorbing rates. Note that for $\chi_u = \chi_v = 0$, Eq. **S7** simplifies to a Neumann boundary condition.

Sporadic random synthesis of PIP3 was introduced as a noise term in Eq. **S6**. The same amount is subtracted from PIP2 to describe its consumption. We set the stochastic events to occur at random positions $\boldsymbol{x}_c$ at rate θ per area. The noise intensity follows a spatial profile $N(\boldsymbol{x}) = N \times \exp(-|\boldsymbol{x} - \boldsymbol{x}_c|^2/2d^2)$, where $\boldsymbol{x}_c$ is

the center of the profile, d is the size of initial nucleation, and N is the noise intensity that follows an exponential distribution with the average σ.

Numerical Simulations in 2D Space with Boundary Deformation. We found that the membrane extension and retraction were highly correlated with the arrival of the wavefront at the cell edge (Fig. S1 *C* and *D*). Most notably, when the waves of PIP3 reached the edge, the corresponding side of the membrane was extended at the speed proportional to the level of PIP3 (Fig. S1 *C*, *Upper Right* and *Lower Left*, and *D*, *Left*). Although there have been some attempts in the past to associate cell morphodynamics with wave dynamics, they have mainly focused either on one-dimensional dynamics along the cell boundary (11, 12, 16) or on 2D patterns in a fixed circular domain (17). Here, to couple the reaction kinetics with a deforming boundary, we adopted a method developed by Shao et al. (18). In this scheme, $\phi(\boldsymbol{x}, t)$ is a function of space $\boldsymbol{x} = (x, y)$ and time t that represents the cell interior as $\phi = 1$ and exterior as $\phi = 0$. By spatially restricting the rate equations (Eq. **S6**) within the boundary, the following equations were derived:

$$\begin{aligned}\frac{\partial(\phi U)}{\partial t} &= D_{\mathrm{U}}\nabla(\phi\nabla U) + \phi\left[-\frac{\alpha UV^2}{K_{\mathrm{K}} + A^{-1}\int \phi V^2 \mathrm{d}x}\right. \\ &\left. + \frac{\beta UV}{K_{\mathrm{P}} + A^{-1}\int \phi U \mathrm{d}x} + S - \gamma U\right] - \chi_{\mathrm{u}}\frac{U|\nabla\phi|^2}{\int |\nabla\phi|^2 \mathrm{d}x} \\ \frac{\partial(\phi V)}{\partial t} &= D_{\mathrm{V}}\nabla(\phi\nabla V) + \phi\left[\frac{\alpha UV^2}{K_{\mathrm{K}} + A^{-1}\int \phi V^2 \mathrm{d}x}\right. \\ &\left. - \frac{\beta UV}{K_{\mathrm{P}} + A^{-1}\int \phi U \mathrm{d}x} - \mu V\right] - \chi_{\mathrm{v}}\frac{V|\nabla\phi|^2}{\int |\nabla\phi|^2 \mathrm{d}x}.\end{aligned} \quad \textbf{[S8]}$$

Here, $A = \int_\Omega \phi \mathrm{d}x$ is the area of a cell, and the last term derives from the boundary condition (Eq. **S7**) (19).

The dynamics of $\phi(\boldsymbol{x}, t)$ describe a cell as an abstract elastic vesicle, where the shape is determined by interactions between the surface tension, pressure, and interior chemical dynamics. Following ref. 18 we solved

$$\tau\frac{\partial\phi}{\partial t} = \eta\left(\Delta\phi - \varepsilon^{-2}G'(\phi)\right) - M\left(\int \phi dx - A_0\right)|\nabla\phi| + \left(aV - bU\right)|\nabla\phi|. \quad \textbf{[S9]}$$

Here, $G(x) = 18\phi^2(1-\phi)^2$ defines a basal potential of ϕ that renders ϕ bistable at 0 and 1. The first term of the right-hand side thus represents effective surface tension of a cell. The second term maintains the area of a cell around A_0 and thus describes effective pressure. The third term takes into account the rate of membrane extension and retraction proportional to the levels of PIP3 and PIP2, respectively (Fig. S1*C*). For details of implementation, see Shao et al. (18) and Kockelkoren et al. (19). Representative results of the simulated dynamics are compared with experimentally observed patterns in Fig. 4 *F–I*. Previous models of actin waves have focused on the physical processes of actin polymerization (20, 21) and membrane protrusions (22–24); however, the exact forms of regulation were abstract. How such details of regulation could be integrated into this simulation framework (25, 26) is an important avenue for future studies.

Parameters Used in Numerical Simulations. To perform numerical simulations of an immobile cell, we used the second-order Runge–Kutta method with time step $\Delta t = 5.0 \times 10^{-4}$. A circular domain was discretized to a triangular lattice grid, and the diffusion terms were calculated by the second difference scheme with $\Delta x = 5.0/31$. The radius of the circle $R = 5.0$. In Fig. 4 *A–D*, parameter values in Eq. **S6** were (*a*) $K_{\mathrm{K}} = 6.0$, (*b*) $K_{\mathrm{K}} = 5.7$, (*c*) $K_{\mathrm{K}} = 4.2$, and (*d*) $K_{\mathrm{K}} = 2.5$, respectively. The other parameters were $D_{\mathrm{U}} = 0.05$, $D_{\mathrm{V}} = 0.20$, $\alpha = 8.0$, $\beta = 2.0$, $K_{\mathrm{P}} = 5.0$, $S = 1.0$, $\gamma = 0.15$, $\mu = 1.0$, $\chi_{\mathrm{u}} = \chi_{\mathrm{v}} = 0.0$, $\theta = 1.5 \times 10^{-2}$, $d = 0.2$, and $\sigma = 0.5$. Computational unit time and length are set to 10 s and 1 μm, respectively. Accordingly, diffusion constants for PIP2 and PIP3 correspond to 0.5 $\mu m^2/s$ and 2.0 $\mu m^2/s$ in line with experimental estimates (27).

Numerical simulations with boundary deformation were performed using the second-order Runge–Kutta method with $\Delta t = 8.0 \times 10^{-5}$ on the discretized square lattice with $\Delta x = 0.1$. Operator ∇ was computed by the central difference scheme. Parameter values for the results shown in Fig. 4 *F–I* are described in Table S1.

Null-Cline Analysis. We studied a null cline of the model equations to understand how excitability of the system is determined. By taking proper scaling of U and V, we can set $S = 1$ and $\mu = 1$ without losing generality. In the absence of diffusion terms, Eq. **S6** become

$$\begin{aligned}\frac{\mathrm{d}U}{dt} &= -\frac{\alpha UV^2}{K_{\mathrm{K}} + G_{\mathrm{K}}(V)} + \frac{\beta UV}{K_{\mathrm{P}} + G_{\mathrm{P}}(U)} + 1 - \gamma U \\ \frac{\mathrm{d}V}{\mathrm{d}t} &= \frac{\alpha UV^2}{K_{\mathrm{K}} + G_{\mathrm{K}}(V)} - \frac{\beta UV}{K_{\mathrm{P}} + G_{\mathrm{P}}(U)} - V,\end{aligned} \quad \textbf{[S10]}$$

where $G_{\mathrm{K}}(V)$ and $G_{\mathrm{P}}(U)$ represent the global integral terms. First, we studied a case where both $G_{\mathrm{K}}(V)$ and $G_{\mathrm{P}}(U)$ are constant, as this can be exactly shown for steady spiral wave propagation in a circular domain where the integrals are invariant. The equations thus take the following form:

$$\begin{aligned}\frac{\mathrm{d}U}{\mathrm{d}t} &= -\alpha_{\mathrm{s}}UV^2 + \beta_{\mathrm{s}}UV + 1 - \gamma U \\ \frac{\mathrm{d}V}{\mathrm{d}t} &= \alpha_{\mathrm{s}}UV^2 - \beta_{\mathrm{s}}UV - V.\end{aligned} \quad \textbf{[S11]}$$

Here, $\alpha_{\mathrm{s}} = \alpha/(K_{\mathrm{K}} + G_{\mathrm{K}}(V))$ and $\beta_{\mathrm{s}} = \beta/(K_{\mathrm{P}} + G_{\mathrm{P}}(U))$. Fig. S4 *C–E* shows null clines $\mathrm{d}U/\mathrm{d}t = 0$ and $\mathrm{d}V/\mathrm{d}t = 0$ for various α_{s}. A stable fixed point exists at $(U, V) = (1/\gamma, 0) = \mathbf{U}^*$. A perturbation that increases V beyond the right red line in Fig. S4 *C–E* triggered a rapid increase in V and a decrease in U (i.e., acceleration of phosphorylation of PIP2 to PIP3 by the feedback) followed by a large deviating orbit in the U-V plane that settles back to the original fixed point $\mathbf{U}^*$. Therefore, the system is an excitable system in which $\mathbf{U}^*$ is the resting state. The threshold for excitation, Θ_{s}, was evaluated as the smallest increment of V that could trigger such a large excursion in the phase plane. This was given by the distance between the two branches of $\mathrm{d}V/\mathrm{d}t = 0$ from the fixed point in the V direction so that

$$\Theta_{\mathrm{s}} \sim (\beta + \gamma)/\alpha_{\mathrm{s}}. \quad \textbf{[S12]}$$

Note that α_{s} characterizes the strength of the positive feedback. A decrease in the feedback strength increased the threshold hindering creation of new PIP3 waves. On the other hand, by increasing α_{s} another stable fixed point appeared via saddle-node bifurcation (Fig. S4*E*). For a large value of α_s the system was attracted to this new fixed point and the excitable nature of the system was lost. As a result, no wave was observed in the spatially extended system, consistent with what was observed for the *pirA*$^-$ mutant (Fig. 1*G*).

To further study the excitable feature of the system, we analyzed a case where the concentrations of PIP2 and PIP3 are spatially uniform. Eq. **S10** become

$$\frac{dU}{dt} = -\frac{\alpha UV^2}{K_K + V^2} + \frac{\beta UV}{K_P + U} + 1 - \gamma U,$$
$$\frac{dV}{dt} = \frac{\alpha UV^2}{K_K + V^2} - \frac{\beta UV}{K_P + U} - V. \quad \textbf{[S13]}$$

Null clines are shown in Fig. S4 *F–H*. The system again shows excitability, where $(U, V) = \mathbf{U^*}$ is the resting state. The threshold for an excitatory response could be evaluated as

$$\Theta_u \sim \left(\alpha - \sqrt{\alpha^2 - 4\gamma^2 C^2 K_K}\right) \Big/ 2\gamma C, \quad \textbf{[S14]}$$

where $C = (\beta + 1 + K_P)/(\gamma K_P + 1)$. Parameter dependence of the threshold was qualitatively the same as Θ_s. In addition, Fig. S4*H* shows that for large α the system has another stable fixed point that appeared by saddle-node bifurcation. Thus, when the strength of the feedback was too strong, the system again lost its excitability. Taken together, our analyses on a spiral wave and a uniform state both indicated excitability of the system at an intermediate range of feedback strength α. Parameter dependence of the threshold (Eqs. **S12** and **S14**) was consistent with our observations that the rate of wave initiation decreased in pharamacologically treated cells (Fig. 1 *B* and *C* and Fig. S5 *A* and *B*).

Numerical Simulations of a One-Dimensional Wave with a Movable Cell Boundary. To examine how cell deformation affects reflection of PIP3 waves (Fig. 1 *D* and *F*), we studied a one-dimensional system in the absence of noise. A spatial domain $0 \le x \le L_b(t)$ represents a region occupied by a cell, where $L_b(t)$ is the position of the cell edge. Neumann conditions were imposed on both left- ($x = 0$) and right-side ($x = L_b(t)$) boundaries. In the simulation, we set an initial wave that propagates toward the right boundary at $x = L_b(t)$. The position of the boundary $L_b(t)$ moves according to the concentration of PIP3, which was implemented in the same manner as in Eqs. **S8** and **S9** (with $\chi_u = \chi_v = 0$). The stiffness of the boundary depended on several parameters, and here we examined whether the wave was reflected or extinguished at the right-side boundary, depending on the value of a. Larger a indicates more deformable (less stiff) boundary, and $a = 0$ means immovable. Fig. S6*A* is a phase diagram showing whether waves were reflected or extinguished at the boundary, depending on the value of a and K_K (feedback strength from PIP3 to PI3K). Fig. S6*B* shows the simulated wave dynamics at $a = 0.0$, 2.0, and 4.0 ($K_K = 6.1$ and other parameters are described in the figure legend). These results indicate that the effect of membrane deformability is not monotonic; waves reflected at the boundary for the undeformable cell ($a = 0$), but at $a = 2.0$ waves were extinguished at the boundary. For larger values of parameter a, waves were again reflected at the boundary.

1. Fey P, Compton K, Cox EC (1995) Green fluorescent protein production in the cellular slime molds Polysphondylium pallidum and Dictyostelium discoideum. *Gene* 165(1): 127–130.
2. Fischer M, Haase I, Simmeth E, Gerisch G, Müller-Taubenberger A (2004) A brilliant monomeric red fluorescent protein to visualize cytoskeleton dynamics in *Dictyostelium*. *FEBS Lett* 577(1–2):227–232.
3. Schneider N, et al. (2003) A Lim protein involved in the progression of cytokinesis and regulation of the mitotic spindle. *Cell Motil Cytoskeleton* 56(2):130–139.
4. Nellen W, Silan C, Firtel RA (1984) DNA-mediated transformation in Dictyostelium discoideum: Regulated expression of an actin gene fusion. *Mol Cell Biol* 4(12):2890–2898.
5. Buades A, Coll B, Morel J-M (2005) A non-local algorithm for image denoising. *Comput Vis Pattern Recognit* 2:60–65.
6. Simpson DM, Infantosi AF, Rosas DA (2001) Estimation and significance testing of cross-correlation between cerebral blood flow velocity and background electroencephalograph activity in signals with missing samples. *Med Biol Eng Comput* 39(4): 428–433.
7. Skupsky R, Losert W, Nossal RJ (2005) Distinguishing modes of eukaryotic gradient sensing. *Biophys J* 89(4):2806–2823.
8. Sasaki AT, Chun C, Takeda K, Firtel RA (2004) Localized Ras signaling at the leading edge regulates PI3K, cell polarity, and directional cell movement. *J Cell Biol* 167(3): 505–518.
9. Sasaki AT, et al. (2007) G protein-independent Ras/PI3K/F-actin circuit regulates basic cell motility. *J Cell Biol* 178(2):185–191.
10. Iijima M, Huang YE, Luo HR, Vazquez F, Devreotes PN (2004) Novel mechanism of PTEN regulation by its phosphatidylinositol 4,5-bisphosphate binding motif is critical for chemotaxis. *J Biol Chem* 279(16):16606–16613.
11. Arai Y, et al. (2010) Self-organization of the phosphatidylinositol lipids signaling system for random cell migration. *Proc Natl Acad Sci USA* 107(27):12399–12404.
12. Shibata T, Nishikawa M, Matsuoka S, Ueda M (2012) Modeling the self-organized phosphatidylinositol lipid signaling system in chemotactic cells using quantitative image analysis. *J Cell Sci* 125(Pt 21):5138–5150.
13. Weiner OD, Marganski WA, Wu LF, Altschuler SJ, Kirschner MW (2007) An actin-based wave generator organizes cell motility. *PLoS Biol* 5(9):e221.
14. Ruchira, Hink MA, Bosgraaf L, Van Haastert PJ, Visser AJ (2004) Pleckstrin homology domain diffusion in *Dictyostelium* cytoplasm studied using fluorescence correlation spectroscopy. *J Biol Chem* 279(11):10013–10019.
15. Postma M, Bosgraaf L, Loovers HM, Van Haastert PJ (2004) Chemotaxis: Signalling modules join hands at front and tail. *EMBO Rep* 5(1):35–40.
16. Driscoll MK, et al. (2012) Cell shape dynamics: From waves to migration. *PLoS Comput Biol* 8(3):e1002392.
17. Xiong Y, Huang CH, Iglesias PA, Devreotes PN (2010) Cells navigate with a local-excitation, global-inhibition-biased excitable network. *Proc Natl Acad Sci USA* 107(40):17079–17086.
18. Shao D, Rappel WJ, Levine H (2010) Computational model for cell morphodynamics. *Phys Rev Lett* 105(10):108104.
19. Kockelkoren J, Levine H, Rappel WJ (2003) Computational approach for modeling intra- and extracellular dynamics. *Phys Rev E Stat Nonlin Soft Matter Phys* 68(3 Pt 2): 037702.
20. Whitelam S, Bretschneider T, Burroughs NJ (2009) Transformation from spots to waves in a model of actin pattern formation. *Phys Rev Lett* 102(19):198103.
21. Carlsson AE (2010) Dendritic actin filament nucleation causes traveling waves and patches. *Phys Rev Lett* 104(22):228102.
22. Carlsson WE, Mogliner A (2010) Mathematical and physical modeling of actin dynamics in motile cells. *Actin-Based Motility*, ed Carlier MF (Springer, Dordrecht), pp 381–412.
23. Shlomovitz R, Gov NS (2007) Membrane waves driven by actin and myosin. *Phys Rev Lett* 98(16):168103.
24. Enculescu M, Falcke M (2011) Actin-based propulsion of spatially extended objects. *New J Phys* 13:053040.
25. Ziebert F, Swaminathan S, Aranson IS (2012) Model for self-polarization and motility of keratocyte fragments. *J R Soc Interface* 9(70):1084–1092.
26. Shao D, Levine H, Rappel WJ (2012) Coupling actin flow, adhesion, and morphology in a computational cell motility model. *Proc Natl Acad Sci USA* 109(18):6851–6856.
27. Golebiewska U, Nyako M, Woturski W, Zaitseva I, McLaughlin S (2008) Diffusion coefficient of fluorescent phosphatidylinositol 4,5-bisphosphate in the plasma membrane of cells. *Mol Biol Cell* 19(4):1663–1669.

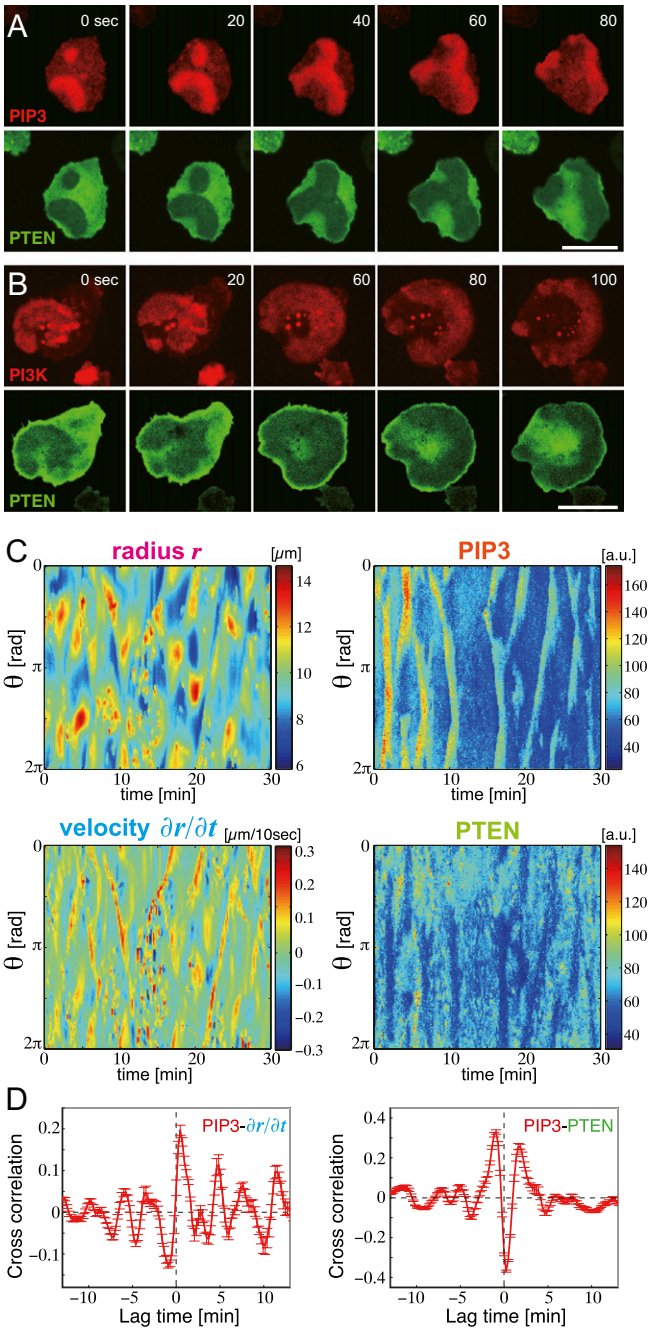

Fig. S1. Wave patterns at the basal membrane and their correlation with the speed of membrane extension at the cell boundary. (*A*) Reciprocal patterns of PIP3 and PTEN-GFP. Extension of the cell edge was observed when PIP3 waves reached the boundary. Conversely, the membrane was retracted at the site enriched in PTEN. (*B*) PI3K (PI3K-RFP) and PTEN at the basal membrane. Spatial patterns of PI3K and PTEN were also mutually exclusive, indicating that wavefronts of PIP3 and PI3K coincide. (Scale bars: 10 μm.) (*C*) (*Upper Left*) Radial distance from the centroid to the edge of a cell in the direction θ. (*Upper Right*) PIP3 accumulation at the cell boundary. (*Lower Left*) Velocity of membrane extension at the boundary in the radial direction. (*Lower Right*) PTEN localization at the cell boundary. Horizontal axis indicates time in minutes and vertical axis represents angle position around the cell border. The amount of PIP3 was positively correlated with the speed of edge expansion and negatively correlated with the level of PTEN. (*D*) (*Left*) Cross-correlation between PIP3 signal intensity at time t and velocity of membrane extension ($\partial r/\partial t$) at time $t + \tau$. (*Right*) Cross-correlation between signal intensities of PIP3 at time t and PTEN at time $t + \tau$ (see *SI Materials and Methods* for details).

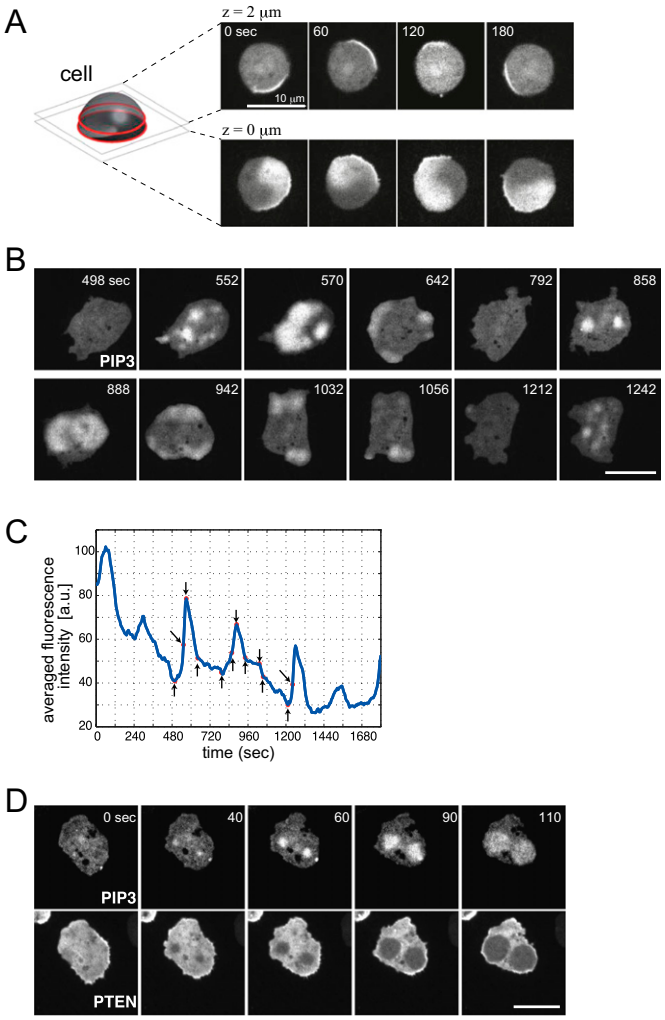

Fig. S2. Wave nucleation. (*A*) PIP3 wave propagation was observed only at the membrane cortex. (*Lower*) A single spiral wave near the glass surface (z = 0 μm). (*Upper*) Images taken from the same cell at a different section ($z = 2$ μm), showing the edge of a rotating wave along the cell boundary but no waves in the cytosol. (*B*) Snapshots of PIP3 waves. Grayscale pixels indicate fluorescence intensity of PHcrac-RFP. PIP3 waves nucleated from several locations simultaneously (Movie S1*B*). (*C*) Time series of the averaged fluorescence intensity in *B*. Arrows indicate time points in *B*. (*D*) Reciprocal patterns of PIP3 and PTEN. The level of PTEN was markedly diminished when PIP3 was elevated. (*Upper*) Snapshots from a time series showing synchronous PIP3 wave nucleation at two spatial points. (*Lower*) Corresponding PTEN images. (Scale bar: 10 μm.) Time is in seconds.

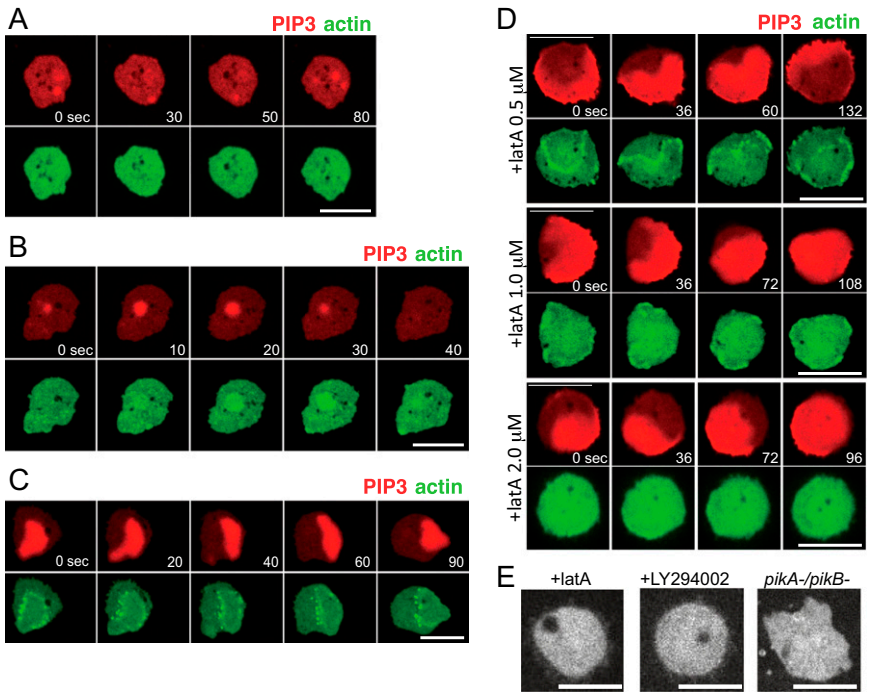

Fig. S3. Propagation of PIP3 and actin waves. PIP3 (PHcrac-RFP) and F-actin (LimEΔCoil-GFP) waves are shown in red and green, respectively. (*A*–*C*) F-actin wave propagation followed accumulation of PIP3 of sufficient duration. (*A*) Sporadic PIP3 accumulation did not give rise to F-actin waves. (*B*) PIP3-enriched focus induced a short-lived F-actin wave. (*C*) Fully developed PIP3 waves propagated together with F-actin waves. (Scale bars: 10 μm.) Time is in seconds. (*D*) PIP3 waves continue to propagate in the absence of F-actin waves. (*Top*) PIP3 (PHcrac-RFP, red) and F-actin (LimEΔCoil-GFP, green) waves in a cell treated with 0.5 μM latrunculin. The waves were well correlated in space. (*Middle*) Patterns of PIP3 and F-actin became less correlated at 1.0 μM latrunculin. (*Bottom*) At 2.0 μM, PIP3 waves propagated in the absence of colocalized F-actin. (Scale bars: 10 μm.) (*E*) Conditions that inhibit PIP3 waves. Treatment with high doses of latrunculin (*Left*, 10 μM) or LY294002 (*Center*, 100 μM) suppressed PIP3 wave formation. A null mutant of PI3K genes *pikA* and *pikB* also did not exhibit PIP3 waves (*Right*). (Scale bars: 10 μm.)

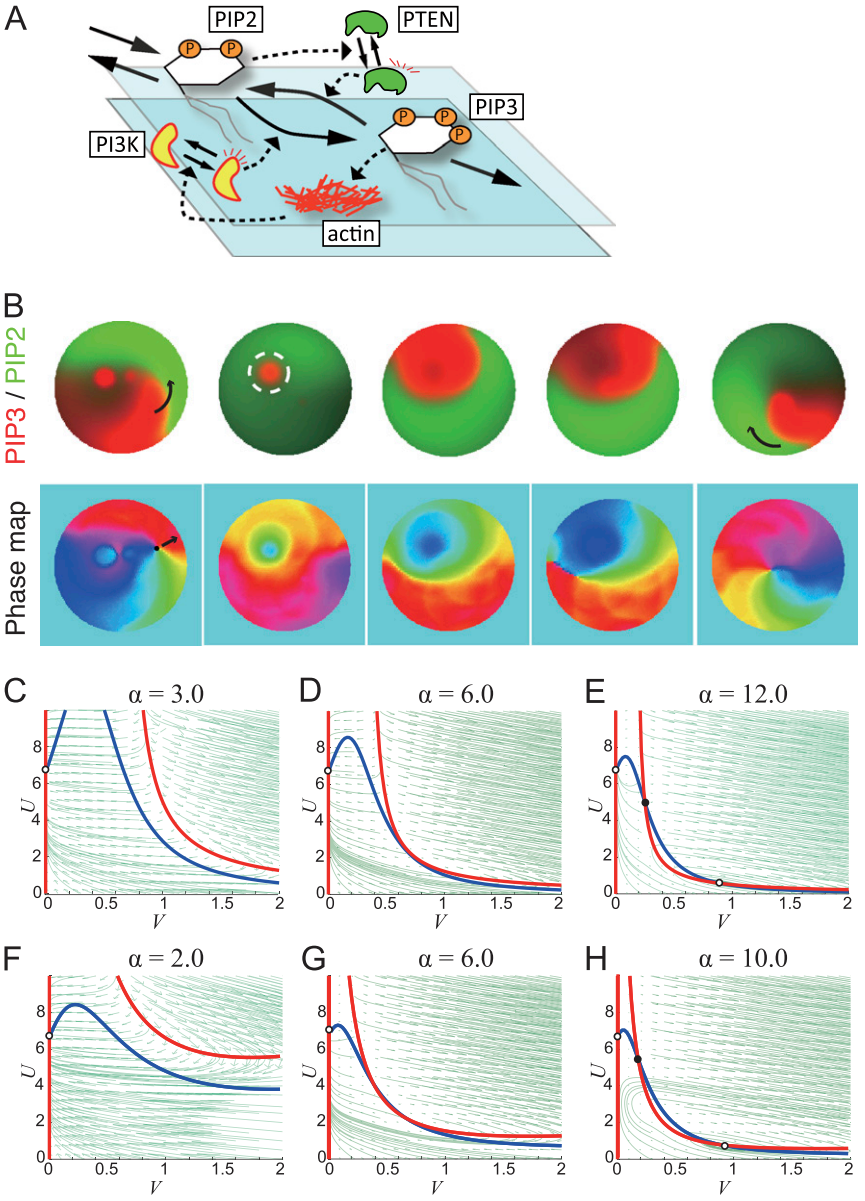

Fig. S4. Model analyses of PIP2-PIP3 reaction dynamics. (*A*) Schematic of reaction steps in the model. PI3K translocates from the cytosol to the membrane and catalyzes phosphorylation of PIP2 to PIP3. The model incorporates a positive feedback loop from PIP3 to PI3K that enhances this reaction. The molecular identity of the feedback is not clear but this study and other studies suggest that it is mediated by F-actin (1, 2). The reverse reaction from PIP3 to PIP2 is catalyzed by phosphatase PTEN, which also translocates from the cytosol to the membrane by binding to PIP2 (3). (*B*) Simulation results showing reversal of spiral waves. (*Upper*) Concentrations of PIP3 (red) and PIP2 (green) in the numerical simulation (time from left to right). (*Lower*) Corresponding time evolution of phase map. At first, a single spiral wave rotated in the counterclockwise direction. The phase singularity disappeared at the edge after meandering. Wave nucleation in the refractory region of a preexisting wave created a pair of phase singularities. The resulting phase singularities repelled from each other and one of them was extinguished after reaching the cell boundary. The remaining phase singularity of +1 charge supported a spiral wave rotating in the clockwise direction. Parameters: $D_U = 0.5$, $D_V = 0.5$, $\alpha = 12.0$, $K_K = 5.0$, $\beta = 1.8$, $K_P = 0.1$, $S = 1.0$, $\gamma = 0.05$, $\mu = 1.6$, $\chi_u = \chi_v = 2.0$, $\theta = 4.0 \times 10^{-3}$, $d = 0.07$, and $\sigma = 1.4$. (*C–H*) Null clines for Eqs. **S11** (*C–E*) and **S13** (*F–H*) are shown for several values of parameter α. Blue lines, $dU/dt = 0$; red lines, $dV/dt = 0$. Open and solid circles represent stable and unstable fixed points, respectively. For small value of α_s (α), $\mathbf{U^*} = (1/\gamma, 0)$ was the only fixed point, and hence the system was not excitable (*C* and *F*). As α was increased, the system exhibited excitability to suprathreshold perturbation to PIP3 production (*D* and *G*). Further increase in α gave rise to a new stable fixed point that appeared by saddle node bifurcation, and the excitability of the system was lost. $\alpha = 3.0$ (*C*), 6.0 (*D*), and 12.0 (*E*) for $K_K = 3.0$, $G_K = 2.0$, $\beta = 2.0$, $K_P = 2.0$, $G_P = 3.0$, and $\gamma = 0.15$. $\alpha = 2.0$ (*F*), 6.0 (*G*), and 10.0 (*H*) for $\beta = 3.0$, $K_K = 3.0$, $K_P = 2.0$, and $\gamma = 0.15$.

1. Sasaki AT, Chun C, Takeda K, Firtel RA (2004) Localized Ras signaling at the leading edge regulates PI3K, cell polarity, and directional cell movement. *J Cell Biol* 167(3):505–518.
2. Kunida K, Matsuda M, Aoki K (2012) FRET imaging and statistical signal processing reveal positive and negative feedback loops regulating the morphology of randomly migrating HT-1080 cells. *J Cell Sci* 125(Pt 10):2381–2392.
3. Iijima M, Huang YE, Luo HR, Vazquez F, Devreotes PN (2004) Novel mechanism of PTEN regulation by its phosphatidylinositol 4,5-bisphosphate binding motif is critical for chemotaxis. *J Biol Chem* 279(16):16606–16613.

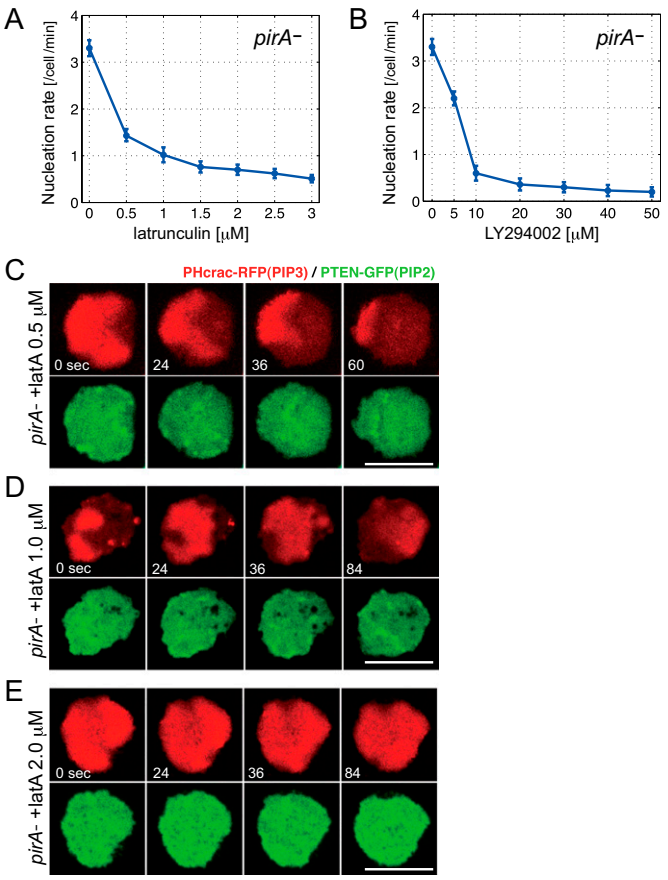

Fig. S5. PIP3 waves in *pirA*$^{-}$ cells. (*A* and *B*) Occurrence of PIP3 waves was markedly enhanced (approximately ninefold compared with wild-type cells; Fig. 1 *B* and *C*) in *pirA*$^{-}$ cells. Treatment with latrunculin (*A*) or LY294002 (*B*) decreased nucleation rate in a dose-dependent manner. (*C*–*E*) PIP3 (PHcrac-RFP, red) waves were restored in latrunculin-treated *pirA*$^{-}$ cells (*C*, 0.5 μM latrunculin). At higher dosages, patterns of PIP3 and F-actin (LimEΔCoil-GFP, green) became less correlated (*D*, 1.0 μM; *E*, 2.0 μM). (Scale bars: 10 μm.) Time is in seconds.

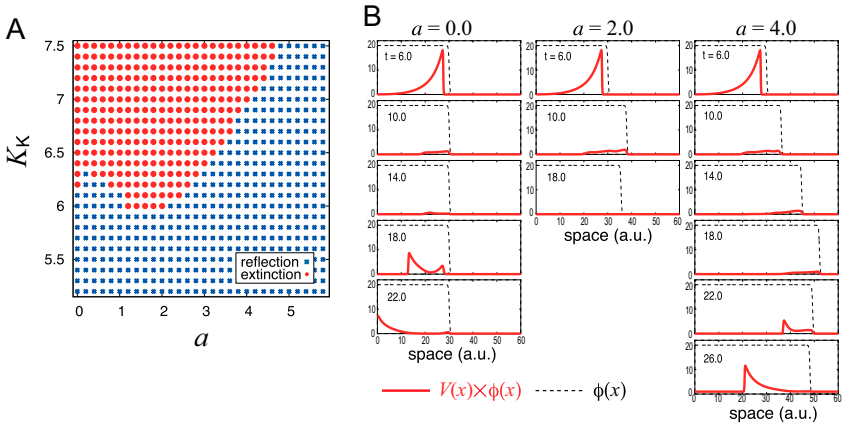

Fig. S6. Analysis of wave reflection and extinction in one-dimensional space. (*A*) Phase diagram of wave reflection as a function of a and K_K. (*B*) Spatio-temporal profile of a wave reflected at nondeformable (*Left*, $a = 0.0$) and highly deformable (*Right*, $a = 4.0$) boundaries. Attenuation of a wave is shown at intermediate values of a (*Center*, $a = 2.0$). Simulations were carried out by a fourth-order Runge–Kutta method with $\Delta x = 0.05$ and $\Delta t = 0.0002$. The other parameters are $D_U = 0.1$, $D_V = 0.4$, $\alpha = 8.0$, $\beta = 1.5$, $S = 1.0$, $\gamma = 0.05$, $K_K = 0.4$, $K_P = 2.0$, $\mu = 1.0$, $\tau = 0.83$, $\varepsilon = 1.0$, $\eta = 1.0$, $M = 0.2$, and $b = 0.0$. Initial conditions $L_b(0) = 25.0$, and A_0 is set as $A_0 = L_b(0)$. The value of K_K was also varied to obtain A.

Table S1. Parameter values used in the numerical simulations in Fig. 4 *F–I*

Parameters	Fig. 4*F*	Fig. 4*G*	Fig. 4*H*	Fig. 4*I*
Eq. **S8**				
α	8.0	12.0	12.0	12.0
β	4.8	3.0	4.0	5.0
K_K	3.5	5.8	6.0	6.0
K_P	5.2	3.0	3.0	2.8
γ	0.15	0.28	0.15	0.20
μ	1.0	1.0	1.0	1.0
χ_u	50.0	80.0	50.0	50.0
χ_v	50.0	80.0	50.0	50.0
Eq. **S9**				
a	10.0	14.0	12.0	12.0
b ($\times 10^{-2}$)	3.0	3.0	3.0	3.5
Random firing of PIP3				
θ ($\times 10^{-3}$)	1.0	1.0	1.0	0.85
d ($\times 10^{-1}$)	0.7	0.6	0.7	1.0
σ	5.7	7.3	5.7	4.0

α and K_K, parameters for PI3K-mediated phosphorylation; β and K_P, parameters for PTEN-mediated dephosphorylation; γ and μ: degradation rate of PIP2 and PIP3; χ_u and χ_v, degradation rate of PIP2 and PIP3 at the boundary. *a*, extension rate of the boundary; *b*, retraction rate of the boundary; θ, rate of stochastic firing. *d*, size of noise profile; σ, intensity of the noise. Other parameters are fixed at $D_U = 0.05$, $D_V = 0.20$ (diffusion constants of PIP2 and PIP3), $S = 1.0$ (rate of PIP2 supply), $\tau = 0.83$, $\varepsilon = 1.0$, $\eta = 1.0$, $M = 0.5$, and $A_0 = 5.0^2 \times \pi$ (parameters for cell boundary change; Eq. **S9**).

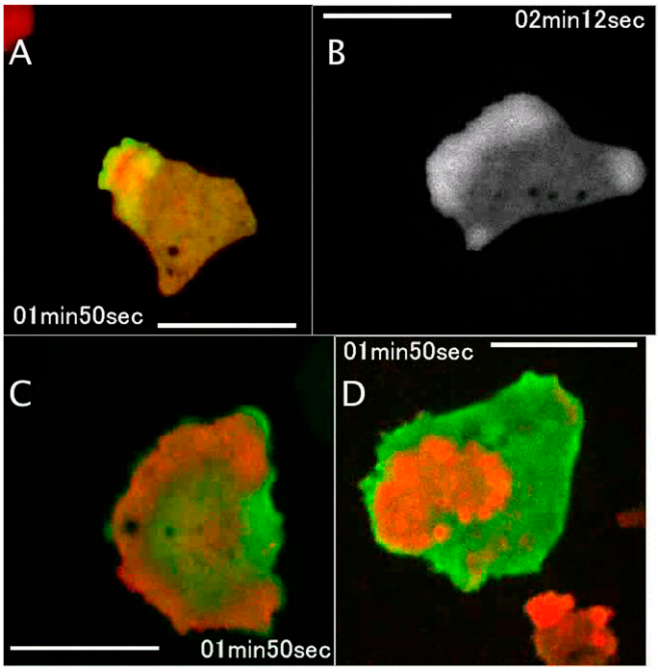

Movie S1. Wave dynamics of PIP3, F-actin, PTEN, and PI3K. (*A*) PIP3 and F-actin waves at the basal membrane: PIP3 (PHcrac-RFP in red) and F-actin (LimEΔcoil-GFP in green) localization. Snapshots are shown in Fig. 1*A*. (*B*) Synchronous nucleation and growth of PIP3 waves. Nucleations of PIP3 waves sometimes occurred synchronously at 3–5 min periodicity. Grayscale pixels indicate fluorescence intensity of PHcrac-RFP. Snapshots are shown in Fig. S2*B*. (*C*) PIP3 (PHcrac-RFP in red) and PTEN (PTEN-GFP in green) localization. Snapshots are shown in Fig. S1*A*. (*D*) PI3K (PI3K-RFP in red) and PTEN (PTEN-GFP in green) localization. Snapshots are shown in Fig. S1*B*. (Scale bars: 10 μm.)

Movie S1

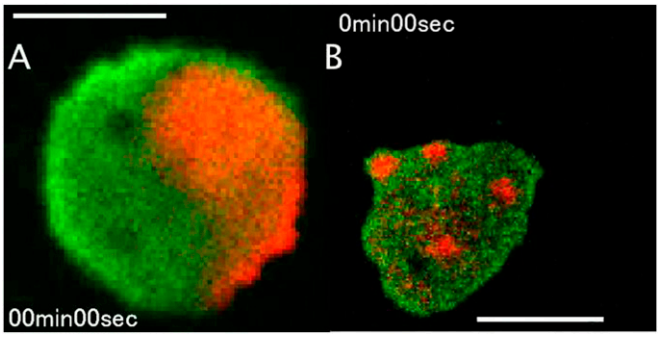

Movie S2. Effect of F-actin on PIP3 waves. (*A*) A single spiral wave in a cell treated with 5 μM latrunculin A. Red and green indicate fluorescence intensity of PHcrac-RFP and PTEN-GFP, respectively. Snapshots are shown in Fig. 1*E*. (Scale bar: 5 μm.) (*B*) PIP3 waves in *pirA*$^{-}$ cells. Patches of sporadic PIP3 accumulation are observed in a *pirA*$^{-}$ cell. Red and green indicate fluorescence intensity of PHcrac-RFP and PTEN-GFP, respectively. Snapshots are shown in Fig. 1*G*. (Scale bar: 10 μm.)

Movie S2

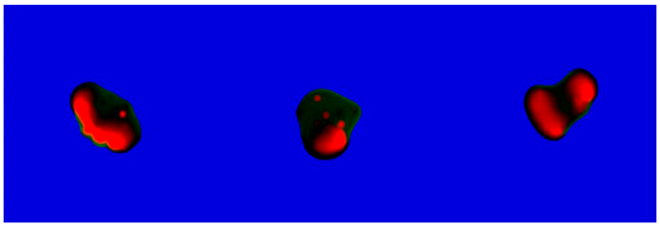

Movie S3. Model simulation of membrane deformation and phosphoinositide waves. Geometry of PIP3-PIP2 waves governs complex morphological dynamics. A transient wave followed by a head-to-head collision and spiral wave formation are seen in these examples. Red and green indicate the concentrations of PIP3 and PIP2, respectively. Parameters are set as follows: (*Left*) $\alpha = 12.0$, $\beta = 2.5$, $K_K = 5.8$, $K_P = 2.8$, $\gamma = 0.18$, $\mu = 1.5$, $\chi_u = \chi_u = 50.0$, $a = 42.0$, $b = 0.03$, $\theta = 1.7 \times 10^{-3}$, $d = 0.08$, and $\sigma = 7.7$; (*Center*) $\alpha = 12.0$, $\beta = 2.5$, $K_K = 4.8$, $K_P = 2.8$, $\gamma = 0.28$, $\mu = 1.3$, $\chi_u = \chi_u = 60.0$, $a = 35.0$, $b = 0.15$, $\theta = 1.7 \times 10^{-3}$, $d = 0.08$, and $\sigma = 7.5$; and (*Right*) $\alpha = 10.0$, $\beta = 3.5$, $K_K = 3.5$, $K_P = 3.2$, $\gamma = 0.32$, $\mu = 1.0$, $\chi_u = \chi_u = 0.0$, $a = 35.0$, $b = 0.09$, $\theta = 1.4 \times 10^{-3}$, $d = 0.08$, and $\sigma = 7.5$. The other parameters are fixed at $D_U = 0.05$, $D_V = 0.20$, $S = 1.0$, $\tau = 0.83$, $\varepsilon = 1.0$, $\eta = 1.0$, $M = 0.5$, and $A_0 = 5.0^2 \times \pi$.

Movie S3